Self-assembled dynamic perovskite composite cathodes for intermediate temperature solid oxide fuel cells

J. Felix Shin[†], Wen Xu[†], Marco Zanella[†], Karl Dawson[‡], Stanislav N. Savvin[†], John B. Claridge*[,†] and Matthew J. Rosseinsky*[,†]

[†]Department of Chemistry, University of Liverpool, Liverpool L69 7ZD, United Kingdom

[‡]School of Engineering, University of Liverpool, Liverpool L69 3GH, United Kingdom

m.j.rosseinsky@liv.ac.uk; j.b.claridge@liv.ac.uk

Electrode materials for intermediate temperature solid oxide fuel cells require electrical and mechanical stability to maintain performance during the cell lifetime. This has proven difficult to achieve for many candidate cathode materials and their derivatives. Here we present $Ba_{0.5}Sr_{0.5}(Co_{0.7}Fe_{0.3})_{0.6875}W_{0.3125}O_{3-\delta}$ (BSCFW), a self-assembled composite prepared through simple solid state synthesis, consisting of B-site cation-ordered double and -disordered single perovskite oxide phases. These phases interact by dynamic compositional change at the operating temperature, promoting both chemical stability through the increased amount of W in the catalytically active single perovskite provided from the W-reservoir double perovskite, and microstructural stability through reduced sintering of the supported catalytically active phase. This interactive catalyst-support system enabled stable high electrochemical activity through the synergic integration of the distinct properties of the two phases.

Solid oxide fuel cells (SOFCs) have attracted considerable research and commercial interest for use as auxiliary power, stationary power and combined heat and power systems owing to their high efficiency, further improved through utilisation of the waste heat[1-4]. To avoid the construction and durability issues that accompany the high operating temperatures of conventional SOFCs, it is desirable to lower the operating temperature to below 700 °C[4-7]. To achieve this goal, research effort has concentrated on novel cathode materials, as conventional cathode materials such as $La_{0.6}Sr_{0.4}MnO_3$ (LSM) show relatively high area specific resistance (ASR) compared to available anode materials (*e.g.,* Ni cermets)[5,8]. Among the candidate cathode materials, BSCF ($Ba_{0.5}Sr_{0.5}Co_{0.8}Fe_{0.2}O_{3-\delta}$) exhibits one of the lowest ASR values at intermediate temperature (IT, 500 – 700 °C), satisfying the required ASR of ≤ 0.1 Ω cm^2 for application at ≈ 600 °C[9,10]. However, it suffers from various stability issues including decomposition to a hexagonal phase at typical operating temperatures (≈ 600 °C) [11,12], reaction with CO_2 to form carbonates when air is used as an oxidant[13,14], reaction with ceria-based electrolytes at cell fabrication conditions (typically at 900 – 1000 °C)[15] and higher thermal expansion coefficients (TEC) (≈ 20 x 10^{-6} K^{-1})[16,17] compared to those of typical electrolytes (≈ 12 x 10^{-6} K^{-1})[18,19], thus preventing practical use.

We have shown that some of these issues can be overcome by the formation of a nanocomposite induced by incorporation of Mo into the perovskite structure of BSCF, where regions of B-site cation order ($A_2BB'O_6$ double perovskite, DP) and disorder (ABO_3 single perovskite, SP) co-exist within a single contiguous AO_3 domain (**Figure 1a, b**). These self-assembled, endotaxial nanocomposite materials (*e.g.,* BSCFMo: $Ba_{0.5}Sr_{0.5}Co_{0.5}Fe_{0.125}Mo_{0.375}O_{3-\delta}$) showed excellent resistance towards decomposition to the hexagonal phase and against reaction with CO_2, while retaining low ASR values which were explained by the synergy between the two phases[11]. However, these systems were not fully compatible with the electrolyte material, samarium doped ceria (SDC), forming 2 weight % $(Ba/Sr)MoO_4$ when fired pelletised with SDC at 950 °C. This scheelite phase, which contains MoO_4^{2-} tetrahedra, also appeared in the phase diagram at compositions rich in Mo and/or Fe[11]. Among the other possible substituents to stabilise such nanocomposite structures, W has the same charge and

similar size (0.60 Å for W^{6+}, 0.59 Å Mo^{6+})[20] but shows a stronger preference towards octahedral geometry in its oxide chemistry than does Mo^{6+} (*e.g.* WO_3 features octahedral W^{6+} whereas Mo^{6+} is five co-ordinate in MoO_3)[21]. We therefore investigated W^{6+} substitution into BSCF at sufficient concentration to form SP/DP composites (aiming to exceed the < 3% limit in the single phase SP-only materials reported to date[22]) motivated by its potential preference for the higher oxide coordination number octahedral perovskite B-site over tetrahedral coordination in the competitor phase scheelite (Ba/Sr)WO_4.

Phase stability

As the samples with a Co:Fe = 8:2 ratio exhibited the lowest ASR in the Mo-doped series, the $Ba_{0.5}Sr_{0.5}(Co_{0.8}Fe_{0.2})_{1-z}W_zO_{3-\delta}$ series ($0.063 \leq z \leq 0.45$) was prepared and characterised initially (blue dashed line in **Figure 1c**)[11]. Their laboratory X-ray diffraction (XRD) patterns showed the coexistence of BSCF-type single (SP) and $BaSrCoWO_6$-type double perovskite (DP) phases with no impurities. The initial screening criteria were ASR of < 0.1 Ω cm^2 at 650 °C and high thermal stability: the z = 0.40 sample satisfied both criteria as it has ASR of 0.063(1) Ω cm^2 and showed no evidence of the hexagonal phase when annealed in static air at 750 °C for 10 days (Supplementary Figure 1). However, the z = 0.3125 sample showed the lowest ASR of 0.034(2) Ω cm^2 in the series, almost half of that of z = 0.40 while showing slower and significantly reduced formation of the hexagonal phase than BSCF upon the same thermal treatment (Supplementary Figure 2).

The stability of $Ba_{0.5}Sr_{0.5}Co_{1-x}Fe_xO_{3-\delta}$ materials in oxidising atmospheres at 700 °C increases with higher Fe content[12]. In order to couple the ASR performance of z = 0.3125 with enhanced stability, the $Ba_{0.5}Sr_{0.5}(Co_{1-x}Fe_x)_{0.6875}W_{0.3125}O_{3-\delta}$ series ($0.2 \leq x \leq 0.5$) was then prepared and characterised (red dashed line in Figure 1c). The increased Fe content improved the thermal stability as there was no evidence of the emergence of the hexagonal peaks for $x \geq 0.3$. The ASR performance deteriorated

when the Fe content was too high (*i.e.* 0.042(1) Ω cm^2 at 650 °C for x = 0.35). The composition $Ba_{0.5}Sr_{0.5}(Co_{0.7}Fe_{0.3})_{0.6875}W_{0.3125}O_{3-\delta}$ (BSCFW) combines thermal stability (**Figure 2a**) with low ASR (0.034(1) Ω cm^2 at 650 °C). Further screening of several compositions around BSCFW (compositions inside the dashed circle on Figure 1c, ASR values and thermal stability data Supplementary Table 1 and Supplementary Figure 3) indicated that this is the optimised composition in terms of cathode performance and thermal stability. Further characterisation was thus concentrated on this BSCFW SP/DP material.

Crystal structure of BSCFW

Combined Rietveld refinement using room temperature (RT) synchrotron X-ray and time-of-flight neutron diffraction data (**Figure 3a**) revealed the crystal structures of the SP and DP phases in BSCFW (for full details of the refinement see Supplementary Note 1). The A-site cations are completely disordered in both SP and DP. Both SP and DP adopt cubic symmetry with lattice parameters of a_p = 3.9770(1) and $2a_p$ = 8.0072(2) Å respectively. The mismatch strain of the two phases is 0.74%. BSCFW consists predominantly of the DP phase (70.7(4) wt.%) with the refined composition $Ba_{0.5}Sr_{0.5}(Co_{0.424(6)}Fe_{0.075(6)})(W_{0.447(9)}Fe_{0.055(6)})O_3$ (**Table 1**), retaining stoichiometric oxygen content. Like BSCFMo, the SP and DP phases in BSCFW have the same AO_3 network characteristic of perovskite while the B-site ordering of the DP is driven by the charge difference between W^{6+} and Co^{2+}, with a small amount of Fe present on both sites. The DP is expected to be a pure electronic conductor based on the stoichiometric oxygen content and mean Co oxidation state of +2.21 (using the oxidation states of W^{6+} and Fe^{3+} as found in BSCFMo[11]: lower iron oxidation states are typically difficult to access in perovskites in air).

The SP phase has the refined composition $Ba_{0.5}Sr_{0.5}Co_{0.59(1)}Fe_{0.354(9)}W_{0.056(3)}O_{2.30(2)}$. The oxygen vacancy content of 23.2(7)% is at the higher end of those reported for BSCF (10.7(2) - 22.3(13)%)[23,24] and is

consistent with the SP phase being a mixed conductor. The SP W content of 5.6(3)% is greater than the typical < 3% solubility limit of W in SP-only BSCF-type materials[22]. This increased solubility can be attributed to the SP/DP composite nature of BSCFW, accessed at the higher synthesis temperature of 1200 °C for BSCFW compared to that used (≈1000 °C) for doped SP BSCF, which is expected to increase the extent of solid solution through entropy-driven disordering in the SP coupled with connection to the DP phase with increased W content. The Co:Fe ratio in the SP phase of nearly 6:4 gives it a higher Fe content than the nominal 7:3 because the B site-ordered DP has a high Co^{2+} content to charge balance its ≈ 45% W^{6+} content.

Diffraction data from 400 to 800 °C show that the SP weight fraction increases with temperature (Supplementary Figure 6), indicating enhanced B-site cation disorder. Combined Rietveld refinement of synchrotron X-ray and time-of-flight neutron diffraction data collected in flowing air at 600 °C (so as to emulate the IT-SOFC operating conditions) to enable full structural analysis revealed significant changes from the RT model (**Figure 3b** and **Table 1**). The refined compositions of the DP and SP phases are $Ba_{0.5}Sr_{0.5}Co_{0.406(6)}Fe_{0.093(6)}W_{0.465(8)}Fe_{0.036(6)}O_3$ and $Ba_{0.5}Sr_{0.5}Co_{0.588(8)}Fe_{0.318(7)}W_{0.094(4)}O_{2.33(2)}$ respectively: the DP oxygen content remains stoichiometric. The SP weight fraction increases from 29.3(2)% at RT to 35.7(2)%. Consequently, the W content of the SP phase increased from 5.6(3) at RT to 9.4(4)% to accommodate the large original RT W content of the DP which becomes more disordered at 600 °C (full details of the SP W content change are given in Supplementary Note 2). This self-balance of the SP/DP system in response to the change in the environment is moderated by the Fe, which changes concentration in both SP and DP phases: from 35.4(9)% at RT to 31.8(7)% at 600 °C in SP to accommodate the increase in W content and from 7.5(6)% to 9.3(6)% at the DP Co/Fe B-site. On the other hand, the amount of Co in both phases showed little deviation from the RT model, as Co occupies approximately half the B-sites for both SP and DP phases. Surprisingly, the oxygen vacancy content of the SP phase did not increase (23.2(7) *vs.* 22.3(6)%), contrary to many BSCF studies where high temperature entropy-driven oxygen loss is enabled by Co reduction[25]. This is because the increased W content of the SP phase at 600 °C pins the oxygen content with its high

formal charge. Overall, these structural changes indicate that the two phases in BSCFW are not isolated but rather interact to accommodate the changes in the environment of the composite, reinforcing its thermal and chemical stability through dynamical self-balancing of the SP/DP system.

No evidence was found for endotaxial intergrowth of the SP and DP phases in a single crystallite which was the key microstructural feature of BSCFMo[11]. BSCFW exhibits an intimately mixed two phase microstructure of the SP and DP (easily distinguished by W content and electron diffraction), and several SP/DP crystallite interfaces show coherent quasi-epitaxial interfaces (**Figure 4**). This spatial phase separation results from the lattice mismatch strain of BSCFW at RT of 0.74%, an order of magnitude greater than 0.095% for BSCFMo, though still consistent with the formation of coherent interfaces between crystallites. The rate of cell expansion of the SP is greater than that of the DP from 400 to 800 °C, but the mismatch strain at 600 °C is still 0.55%. The lattice parameter difference between the phases decreases further at higher temperature (Supplementary Figure 7) and they are extrapolated to coincide at ≈ 1300 °C. The extrapolated mismatch strain at the synthesis temperature of 1200 °C is 0.097%. It is thus possible that endotaxial SP/DP intergrowth of BSCFW occurs under the synthesis conditions enabled by this small strain, which increases on cooling to drive the two phases into distinct crystallites.

ASR and Stability of BSCFW

To assess the suitability of BSCFW as a practical IT-SOFC cathode, ASR values were measured for a symmetrical cell of BSCFW fabricated on an SDC electrolyte from 550 to 700 °C (**Figure 5a**). These ASR are about 3 times lower than that of the best BSCFMo material (0.034(1) Ω cm^2 compared to 0.13 Ω cm^2 at 650 °C) and are comparable with those reported for BSCF (from 0.03 to 10 Ω cm^2 at 650 °C; our in-house measured value is 0.13(1) Ω cm^2 at 650 °C)[9,11,26]. The activation energy of BSCFW is 139(3) kJ mol^{-1}, a slight increase from 116 kJ mol^{-1} of BSCF which was associated with the

surface exchange process[9]. This increased activation energy is commonly seen in doped BSCF studies and is rationalised by the reduced amount of highly oxygen reduction reaction (ORR) active Co and Fe species[27].

Maintaining these low ASR values during SOFC operation is also very important, and requires both thermal and chemical stability of the cathode material. BSCF is well-known to suffer significantly in these areas, thus eliminating it from the practical SOFC application, despite its enhanced cathode performance. BSCFW proved superior to BSCF in a range of stability tests chosen based on the literature and advice from SOFC industry experts. Evaluation of compatibility with SDC at a fabrication temperature of 950 °C for 3 hours, against decomposition to the hexagonal phase in static air at 750 °C for 10 days, reactivity with CO_2 in flowing 1% CO_2 in Ar at 650 °C for 5 days and reactivity with vaporised Cr from steel 316 (*i.e.* typical interconnect material) fired at 850 °C delivered by flowing humid air while BSCFW was held at 650 °C for 7 days (Supplementary Figure 9) were all performed. The SP/DP structure was retained in all cases, showing no significant change in the diffraction patterns and no emergence of any secondary phase (Figure 2a). BSCFW also has the TEC value of 15 x 10^{-6} K^{-1} which is closer to 12 x 10^{-6} K^{-1} of SDC than BSCF (Supplementary Figure 10).

The improved stability of BSCFW is attributed to the high W content of the SP phase in the composite: a single phase SP sample with lower RT W content (2% W-doped BSCF, $Ba_{0.5}Sr_{0.5}Co_{0.78}Fe_{0.2}W_{0.02}O_{3-\delta}$) decomposed to form (Ba/Sr)CO_3 in the CO_2 reactivity test. (Supplementary Figure 11). The W content of the active SP phase at 600 °C is increased over that at RT by cation exchange with the W-reservoir DP, to further enhance the stability of the BSCFW composite. However, BSCFW retains the ASR values similar to undoped BSCF, whereas most doped BSCFs suffer from the loss of transport properties due to the lack of oxygen vacancies[28]. This is particularly unusual as the majority DP phase in BSCFW is expected to have inferior oxide ion transport properties than the SP, because the W^{6+} content prevents vacancy formation. The DP alone thus shows far higher ASR than the BSCFW composites when measured in isolation: 7.1(2) and

1.0(1) Ω cm^2 at 650 °C for the stoichiometric double perovskite, $BaSrCoWO_6$ and the refined DP composition of BSCFW, $BaSrCo_{0.85}Fe_{0.26}W_{0.89}O_6$ (*i.e.* Fe-doped $BaSrCoWO_6$) respectively.

The DP phase in BSCFMo was not a simple spectator, but contributed to the ORR performance synergically, most significantly through electron transport[11]. The same co-operative DP/SP effect is expected in BSCFW. The composite has an improved cathode microstructure, observed by SEM (**Figure 5c and d**). After sintering at 950 °C for 3 hours, BSCFW exhibited greater porosity (33%) than BSCF (22%), which showed enhanced particle sintering. This is associated with the presence of the more refractory DP which requires higher synthesis temperature (1200 *vs.* 1000 °C for SP)[9,29] and interacts via coherent interfaces (Figure 4) with the SP particles to inhibit particle growth and retain surface area. Thus the DP provides an inert and rigid platform for the ORR-active mixed conductor SP, which is present above the percolation threshold to enable electron/oxide ion transport to the current collector/electrolyte. This SP/DP arrangement is analogous to a supported (electro)catalyst, where the dispersion of a catalytically active phase is maximised by locating it on a robust support material[30]. For example, in a typical electrode arrangement for polymer electrolyte membrane fuel cells, electrochemically active Pt particles are deposited on a chemically stable and electronically conducting high surface area carbon support to increase the triple phase boundary and lower the ASR[31]: the catalyst-support interaction suppresses agglomeration of Pt by diffusion. Routes to similar morphologies to increase the active surface area have been explored in the IT-SOFC field, but require sophisticated engineering techniques such as impregnation, and often suffer from the subsequent loss of surface area through sintering at IT-SOFC operating temperatures[32,33]. Porosity is retained upon processing in BSCFW because ionic mobility is reduced in the majority DP, which supports the SP and reduces its tendency to sinter via the SP/DP catalyst support interaction (Figure 5).

To clarify whether this supported catalyst type improved morphology can be achieved through the simple composite route, a physically-mixed composite of pre-prepared BSCF and $BaSrCoWO_6$ in

30:70 weight ratio was prepared. The physically-mixed composite cathode showed a similar morphology (34% porosity) to BSCFW (**Figure 5e**), demonstrating the inhibiting effect of the DP on coarsening of the SP phase, and exhibited an ASR (0.066(1) Ω cm^2 at 650 °C) double that of BSCFW but over an order of magnitude less than the DP component in isolation. However, this physically-mixed composite did not show any improvement in chemical stability (to CO_2 or the hexagonal phase) as there was no chemical alteration of BSCF in the physically-mixed composite (Supplementary Figure 12): this demonstrates the key role played by the small but significant W content in the SP phase and the dynamic nature of the SP/DP system which supplies stabilising W^{6+} to the SP from the W-reservoir DP at IT-SOFC operating temperature. This phenomenon is readily accessed by the simple thermal synthesis/processing route described here, as it relies on the thermodynamic phase separation into SP and DP at high W content.

The stability and low ASR of self-assembled composite BSCFW is demonstrated by the extended continuous ASR measurement at 650 °C in static air which showed ASR values of 0.034(1) Ω cm^2 initially and 0.039(2) Ω cm^2 after 60 hours (**Figure 5b**). This indicates that the improved morphology of the supported catalyst is retained. In comparison with commercial BSCF (Praxair Specialty Ceramics) fabricated and measured with the same protocol, BSCFW showed a third of the rate of performance loss. Furthermore, the diffraction pattern taken after this long-term ASR test showed no significant change (**Figure 2b**), demonstrating the thermal and chemical stability of BSCFW. For additional comparison, another typical mixed ionic and electronic conductor (MIEC) cathode material, $La_{0.6}Sr_{0.4}Co_{0.2}Fe_{0.8}O_{3-\delta}$, LSCF (which was measured at 800 °C to achieve comparable ASR of 0.061(1) Ω cm^2) showed the highest degradation rate among the measured samples, decaying four times faster than BSCFW. Further improvement in the ASR stability may arise from approaches such as the selective use of other d^0 species alongside W^{6+} to prevent SP aggregation, and optimisation of cathode processing[34,35].

Conclusions

BSCFW self-assembles into a composite where the stable electronic conductor DP both supports the catalytically active MIEC SP to prevent loss of external surface through aggregation and stabilises the SP through dynamic incorporation of W^{6+} at the IT-SOFC operating temperature to limit the oxygen vacancy content, thus combining low ASR with chemical and microstructural stability via the coherent, quasi-epitaxial interfaces between the phases. In particular, the segregation of W^{6+} into the majority DP phase allows the percolating SP to retain sufficient anion vacancies for transport and electrocatalysis. The high RT Fe content of the SP sets up the subsequent dynamic high temperature exchange of W^{6+} with the DP to limit further oxide loss and disfavour the competing hexagonal phase, whose face-sharing octahedral sites do not suit highly charged B site cations. W^{6+} competes with CO_2 more effectively than lower-charged transition metals in the acid-base reactivity with oxide, suppressing carbonate formation. The preference of W^{6+} in oxide chemistry for octahedral co-ordination checks the formation of the tetrahedron-based scheelite phases that undermine this strategy for Mo^{6+}, despite their equal formal charges and almost identical sizes.

Methods

High purity (≥ 99.9%) $BaCO_3$, $SrCO_3$, Co_3O_4, Fe_2O_3 and WO_3 were used to prepare $Ba_{0.5}Sr_{0.5}(Co_xFe_y)_{1-z}W_zO_{3-\delta}$ samples. The powders were ball-milled overnight in 2-propanol with ZrO_2 balls (350 rpm , Fritsch Pulverisette 7 Planetary Mill), dried and heated initially to 700 °C for 6 hours followed by 900 °C for 8 hours before ball-milling again. The resulting powders were then pressed as pellets (1.3 cm diameter) and sintered at 1200 °C for 12 hours. Phase purity was determined using X-ray powder diffraction (Panalytical X-pert Pro Bragg-Brentano geometry laboratory X-ray diffractometer with Co $K\alpha_1$ radiation = 1.78901 Å). For the detailed structural analysis of $Ba_{0.5}Sr_{0.5}(Co_{0.7}Fe_{0.3})_{0.6875}W_{0.3125}O_{3-\delta}$, synchrotron X-ray diffraction data of powder samples were recorded on Beamline I11 with a wide-angle position sensitive detector(λ = 0.825623 Å) at Diamond Light Source, UK and time-of-flight neutron diffraction data of sintered pellets in a quartz tube under flowing air were recorded on the Polaris diffractometer at the ISIS facility, Rutherford Appleton Laboratories, UK. Structural parameters were refined by the Rietveld method with the Topas software[36] (for full details see Supplementary Note 1).

Thin lamella transmission electron microscopy (TEM) specimens were produced by the lift out method using a focussed (Ga) ion beam (FIB) instrument[37]. TEM was performed using a Schottky field emission gun equipped JEOL JEM 2100FCs microscope operating at 200 kV. Bright field images were collected using conventional TEM illumination and High-Angle Annular Dark Field (HAADF) images were recorded in scanning TEM (STEM) mode using a CEOS aberration corrected probe. Energy-dispersive spectrometry (EDS) measurements were performed in the same instrument using an EDAX windowless silicon drift x-ray detector and TEAM collection/analysis software.

For the preparation of the symmetrical cells for the ASR measurements, the cathode materials were ball-milled in isopropanol overnight followed by further ball-milling with the pore-former V-006 (Heraeus Electronic Materials) for 3 hours, with a mass ratio between cathode materials and the pore-former of 1:0.7. The suspension was then screen-printed onto a sintered samarium doped ceria

(SDC) electrolyte (Fuel cell materials) on both sides (area of ≈ 0.56 cm^2 for each side), and dried in an oven at 100 °C: this was repeated 10 times (4 times for reference cathodes, see Supplementary Note 6 for full detail). The cell was fired to 950 °C for 3 hours, and then coated with Au paste, followed by heating to 600 °C for 1 hour to ensure bonding to the cathode surface. ASR measurements were then performed in static air by AC impedance spectroscopy (Metrohm Autolab AUT84515) in the frequency range from 0.1 to 10^5 Hz with a perturbation of 10 mV. The impedance data were analysed using *ZView* software[38].

References

1. Irvine, J. T. S. *et al.* Evolution of the electrochemical interface in high-temperature fuel cells and electrolysers. *Nature Energy* **1**, 15014, (2016).
2. Yokokawa, H. Towards comprehensive description of stack durability/reliability behavior. *Fuel Cells* **15**, 652-668 (2015).
3. Zhang, X. *et al.* A review of integration strategies for solid oxide fuel cells. *J. Power Sources* **195**, 685-702 (2010).
4. Kilner, J. A. & Burriel, M. Materials for intermediate-temperature solid-oxide fuel cells. *Annual Review of Materials Research* **44**, 365-393 (2014).
5. Aguadero, A. *et al.* Materials development for intermediate-temperature solid oxide electrochemical devices. *J Mater Sci* **47**, 3925-3948 (2012).
6. Lee, K. T. & Wachsman, E. D. Role of nanostructures on SOFC performance at reduced temperatures. *MRS Bull.* **39**, 783-791 (2014).
7. Gao, Z., Mogni, L. V., Miller, E. C., Railsback, J. G. & Barnett, S. A. A perspective on low-temperature solid oxide fuel cells. *Energy Environ. Sci.* **9**, 1602-1644, (2016).
8. Kendrick, E. & Slater, P. R. Battery and solid oxide fuel cell materials. *Annual Reports on the Progress of Chemistry, Section A: Inorganic Chemistry,* **109**, 396-420 (2013).
9. Shao, Z. & Haile, S. M. A high-performance cathode for the next generation of solid-oxide fuel cells. *Nature* **431**, 170-173 (2004).
10. Steele, B. C. H. & Heinzel, A. Materials for fuel-cell technologies. *Nature* **414**, 345-352 (2001).
11. Demont, A. *et al.* Single sublattice endotaxial phase separation driven by charge frustration in a complex oxide. *J. Am. Chem. Soc.* **135**, 10114-10123 (2013).
12. Jung, J.-I. & Edwards, D. X-ray photoelectron study on $Ba_{0.5}Sr_{0.5}CoFe_{1-x}O_{3-\delta}$ (BSCF: x = 0.2 and 0.8) ceramics annealed at different temperature and pO_2. *J Mater Sci* **46**, 7415-7422 (2011).
13. Yan, A. *et al.* Investigation of a $Ba_{0.5}Sr_{0.5}Co_{0.8}Fe_{0.2}O_{3-\delta}$ based cathode IT-SOFC: I. The effect of CO_2 on the cell performance. *Applied Catalysis B: Environmental* **66**, 64-71 (2006).

14. Yan, A., Maragou, V., Arico, A., Cheng, M. & Tsiakaras, P. Investigation of a $Ba_{0.5}Sr_{0.5}Co_{0.8}Fe_{0.2}O_{3-\delta}$ based cathode SOFC: II. The effect of CO_2 on the chemical stability. *Applied Catalysis B: Environmental* **76**, 320-327 (2007).
15. Wang, K. *et al.* Properties and performance of $Ba_{0.5}Sr_{0.5}Co_{0.8}Fe_{0.2}O_{3-\delta}$+$Sm_{0.2}Ce_{0.8}O_{1.9}$ composite cathode. *J. Power Sources* **179**, 60-68 (2008).
16. Patra, H., Rout, S. K., Pratihar, S. K. & Bhattacharya, S. Thermal, electrical and electrochemical characteristics of $Ba_{1-x}Sr_xCo_{0.8}Fe_{0.2}O_{3-\delta}$ cathode material for intermediate temperature solid oxide fuel cells. *Int. J. Hydrogen Energy* **36**, 11904-11913 (2011).
17. Li, S., Lü, Z., Huang, X. & Su, W. Thermal, electrical, and electrochemical properties of Nd-doped $Ba_{0.5}Sr_{0.5}Co_{0.8}Fe_{0.2}O_{3-\delta}$ as a cathode material for SOFC. *Solid State Ionics* **178**, 1853-1858 (2008).
18. Kharton, V. V. *et al.* Ceria-based materials for solid oxide fuel cells. *J Mater Sci* **36**, 1105-1117 (2001).
19. Sameshima, S., Ichikawa, T., Kawaminami, M. & Hirata, Y. Thermal and mechanical properties of rare earth-doped ceria ceramics. *Mater. Chem. Phys.* **61**, 31-35 (1999).
20. Shannon, R. D. & Prewitt, C. T. Effective ionic radii in oxides and fluorides. *Acta Cryst.* **B 25**, 925-946 (1969).
21. Wells, A. F. *Structural Inorganic Chemistry* (Oxford Univ. Press, 1984).
22. Popov, M. P., Starkov, I. A., Bychkov, S. F. & Nemudry, A. P. Improvement of $Ba_{0.5}Sr_{0.5}Co_{0.8}Fe_{0.2}O_{3-\delta}$ functional properties by partial substitution of cobalt with tungsten. *Journal of Membrane Science* **469**, 88-94 (2014).
23. Itoh, T. *et al.* Determination of the crystal structure and charge density of $(Ba_{0.5}Sr_{0.5})(Co_{0.8}Fe_{0.2})O_{2.33}$ by Rietveld refinement and maximum entropy method analysis. *Solid State Commun.* **149**, 41-44 (2009).
24. Chen, Z., Ran, R., Zhou, W., Shao, Z. & Liu, S. Assessment of $Ba_{0.5}Sr_{0.5}Co_{1-y}Fe_yO_{3-\delta}$ (y = 0.0–1.0) for prospective application as cathode for IT-SOFCs or oxygen permeating membrane. *Electrochim. Acta* **52**, 7343-7351 (2007).

25. McIntosh, S., Vente, J. F., Haije, W. G., Blank, D. H. A. & Bouwmeester, H. J. M. Structure and oxygen stoichiometry of $SrCo_{0.8}Fe_{0.2}O_{3-\delta}$ and $Ba_{0.5}Sr_{0.5}Co_{0.8}Fe_{0.2}O_{3-\delta}$. *Solid State Ionics* **177**, 1737-1742 (2006).

26. Lim, Y. H., Lee, J., Yoon, J. S., Kim, C. E. & Hwang, H. J. Electrochemical performance of $Ba_{0.5}Sr_{0.5}Co_xFe_{1-x}O_{3-\delta}$ (x=0.2–0.8) cathode on a ScSZ electrolyte for intermediate temperature SOFCs. *J. Power Sources* **171**, 79-85 (2007).

27. Bi, L., Fabbri, E. & Traversa, E. Novel $Ba_{0.5}Sr_{0.5}(Co_{0.8}Fe_{0.2})_{(1-x)}Ti_xO_{3-\delta}$ (x=0, 0.05, and 0.1) cathode materials for proton-conducting solid oxide fuel cells. *Solid State Ionics* **214**, 1-5 (2012).

28. Fang, S. M., Yoo, C. Y. & Bouwmeester, H. J. M. Performance and stability of niobium-substituted $Ba_{0.5}Sr_{0.5}Co_{0.8}Fe_{0.2}O_{3-\delta}$ membranes. *Solid State Ionics* **195**, 1-6 (2011).

29. Ray, R. *et al.* Electronic structure of ordered double perovskite Ba_2CoWO_6. *AIP Conference Proceedings* **1591**, 1155-1157 (2014).

30. Ma, Z. & Zaera, F. Heterogeneous catalysis by metals. *Encyclopedia of Inorganic Chemistry* (John Wiley & Sons, Ltd, 2006).

31. de Bruijn, F. A., Dam, V. A. T. & Janssen, G. J. M. Durability and degradation issues of PEM fuel cell components. *Fuel Cells* **8**, 3-22 (2008).

32. Shah, M., Voorhees, P. W. & Barnett, S. A. Time-dependent performance changes in LSCF-infiltrated SOFC cathodes: The role of nano-particle coarsening. *Solid State Ionics* **187**, 64-67 (2011).

33. Jiang, S. P. Nanoscale and nano-structured electrodes of solid oxide fuel cells by infiltration: Advances and challenges. *Int. J. Hydrogen Energy* **37**, 449-470 (2012).

34. Tietz, F., Mai, A. & Stöver, D. From powder properties to fuel cell performance – A holistic approach for SOFC cathode development. *Solid State Ionics* **179**, 1509-1515 (2008).

35. Haanappel, V. A. C. *et al.* Optimisation of processing and microstructural parameters of LSM cathodes to improve the electrochemical performance of anode-supported SOFCs. *J. Power Sources* **141**, 216-226 (2005).

36. Coelho, A. A. *TOPAS Academic: General profile and structure analysis software for powder diffraction data* (Bruker AXS, Karlsruhe, Germany 2010).
37. Obst, M., Gasser, P., Mavrocordatos, D. & Dittrich, M. TEM-specimen preparation of cell/mineral interfaces by focused ion beam milling. *Am. Mineral.* **90**, 1270-1277 (2005).
38. Johnson, D. *ZView: a Software program for IES analysis, version 3.1c* (Scribner Associates Inc. 2007).

Correspondence to Matthew J. Rosseinsky (m.j.rosseinsky@liv.ac.uk) and John B. Claridge (j.b.claridge@liv.ac.uk)

Acknowledgments

We thank EPSRC for support under EP/H000925 and EP/N004884. Synchrotron X-ray diffraction work was carried out with the support of Diamond Light Source (UK). Time-of-flight neutron diffraction work was carried out with the support of ISIS Spallation Source (UK). We thank C. Tang, S. Thompson, J. Parker, and P. Adamson for assistance on Beamline I11 (Diamond Light Source) and R. Smith for assistance on POLARIS (ISIS). M.J.R. is a Royal Society Research Professor.

Author Contributions

M.J.R. and J.B.C. developed the concept for the study with input from J.F.S. W.X. performed initial exploratory work with supervision from J.F.S. J.F.S. designed and performed the remaining experiments, with the exceptions of DC conductivity measurement by S.N.S and TEM work performed by K.D. and M.Z. J.F.S. and M.J.R. wrote the first draft, which J.F.S. then expanded. All authors discussed the results and further developed the manuscript.

Competing Financial Interests

A patent application covering this work has been filed by Ceres Intellectual Property Company Limited (UK patent application no. GB1421069.4, International patent application no. PCT/GB2015/053400) that names M.J.R., J.B.C., J.F.S. and W.X. as inventors.

Table 1: Refined parmeters of BSCFW. Structural parameters from combined Rietveld refinement of X-ray and neutron diffraction data of BSCFW, $Ba_{0.5}Sr_{0.5}(Co_{0.7}Fe_{0.3})_{0.6875}W_{0.3125}O_{3-\delta}$ at room temperature and at 600 °C in flowing air.

RT	Double Perovskite Phase (**DP**) $BaSrCo_{0.847(12)}Fe_{0.260(22)}W_{0.891(17)}O_6$, a_0 = 8.0118(2) Å						
	weight fraction 0.707(4), *Fm$\bar{3}$m* (225)						
	atom	multiplicity	x	y	z	occupancy	B_{iso}(Å^2)
	Ba	8c	0.25	0.25	0.25	0.5	0.69(1)
	Sr	8c	0.25	0.25	0.25	0.5	
	W	4b	0.5	0.5	0.5	0.891(17)	0.53(1)
	Fe1	4b	0.5	0.5	0.5	0.110(10)	
	Co	4a	0	0	0	0.847(12)	0.72(3)
	Fe2	4a	0	0	0	0.150(12)	
	O	24e	0.2593(2)	0	0	1	0.75(1)
	Single Perovskite Phase (**SP**) $Ba_{0.5}Sr_{0.5}Co_{0.589(10)}Fe_{0.354(9)}W_{0.056(3)}O_{2.304(21)}$, a_0 = 3.9763(1) Å						
	weight fraction 0.293(2), *Pm$\bar{3}$m* (221)						
	atom	multiplicity	x	y	z	occupancy	B_{iso}(Å^2)
	Ba	1a	0	0	0	0.5	1.26(3)
	Sr	1a	0	0	0	0.5	
	Co	1b	0.5	0.5	0.5	0.589(10)	1.08(4)
	Fe	1b	0.5	0.5	0.5	0.354(9)	
	W	1b	0.5	0.5	0.5	0.056(3)	
	O	3c	0.5	0.5	0	0.768(7)	1.38(5)
600 °C	Double Perovskite Phase (**DP**) $BaSrCo_{0.812(12)}Fe_{0.256(23)}W_{0.929(16)}O_6$, a_0 = 8.0621(1) Å						
	weight fraction 0.643(4), *Fm$\bar{3}$m* (225)						
	atom	multiplicity	x	y	z	occupancy	B_{iso}(Å^2)
	Ba	8c	0.25	0.25	0.25	0.5	1.56(2)
	Sr	8c	0.25	0.25	0.25	0.5	
	W	4b	0.5	0.5	0.5	0.929(16)	1.02(2)
	Fe1	4b	0.5	0.5	0.5	0.071(11)	
	Co	4a	0	0	0	0.812(12)	1.32(4)
	Fe2	4a	0	0	0	0.185(11)	
	O	24e	0.2611(2)	0	0	1	1.60(2)
	Single Perovskite Phase (**SP**) $Ba_{0.5}Sr_{0.5}Co_{0.588(8)}Fe_{0.318(7)}W_{0.094(4)}O_{2.332(18)}$, a_0 = 4.0093(1) Å						
	weight fraction 0.357(2), *Pm$\bar{3}$m* (221)						
	atom	multiplicity	x	y	z	occupancy	B_{iso}(Å^2)
	Ba	1a	0	0	0	0.5	1.75(4)
	Sr	1a	0	0	0	0.5	
	Co	1b	0.5	0.5	0.5	0.588(8)	1.77(4)
	Fe	1b	0.5	0.5	0.5	0.318(7)	
	W	1b	0.5	0.5	0.5	0.094(4)	
	O	3c	0.5	0.5	0	0.774(6)	2.19(4)

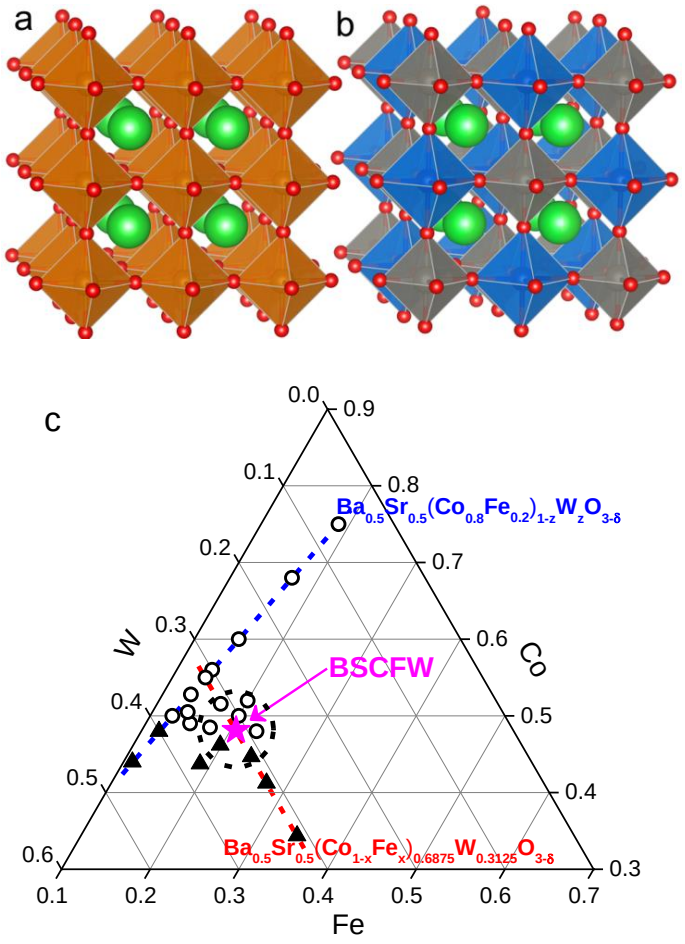

Figure 1: Phase diagram and crystal structure of the composite system. (a) B-site disordered single perovskite (SP) and (b) ordered double perovskite (DP). A-site cations are shown as green spheres while BO_6 octahedra are shown in orange for SP and blue and grey in the rocksalt type ordering for DP in ABO_3 perovskite structure. (c) All the compositions in the phase diagram are SP/DP composites without any additional phases. The blue and red dashed lines indicate $Ba_{0.5}Sr_{0.5}(Co_{0.8}Fe_{0.2})_{1-z}W_zO_{3-\delta}$ and $Ba_{0.5}Sr_{0.5}(Co_{1-x}Fe_x)_{0.6875}W_{0.3125}O_{3-\delta}$ series respectively. The optimised composition, $Ba_{0.5}Sr_{0.5}(Co_{0.7}Fe_{0.3})_{0.6875}W_{0.3125}O_{3-\delta}$ (BSCFW) is marked with a magenta star and other thermally stable compositions are shown with filled triangles: thermally unstable materials are marked with open circle. The ASR values and XRD patterns for the thermal stability tests for the compositions in the dashed circle are shown in Supplementary Table 1 and Supplementary Figure 3.

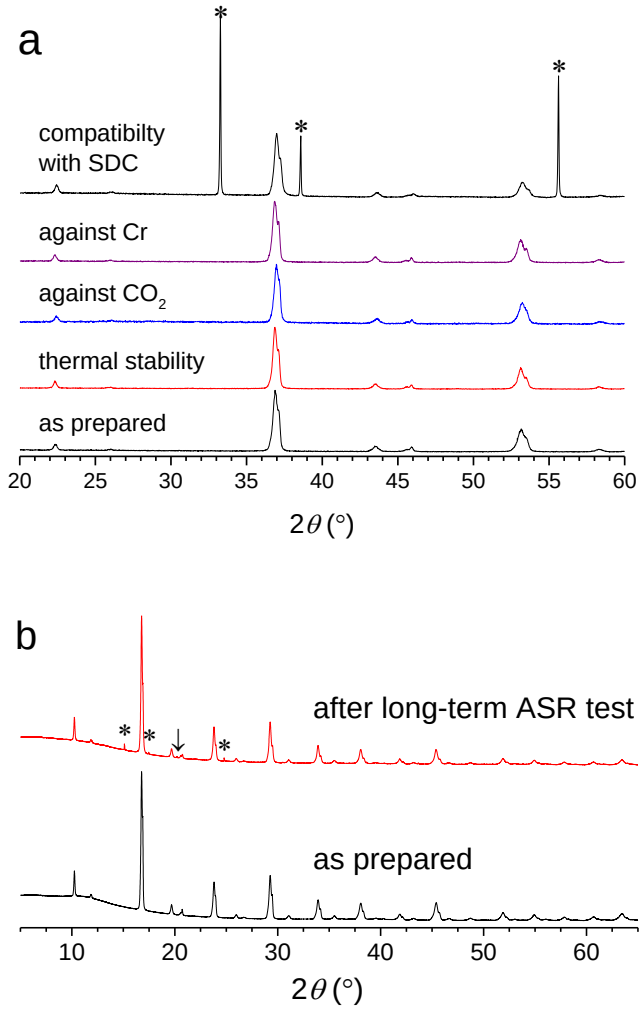

Figure 2: Stability of BSCFW shown by XRD patterns. (a) Laboratory XRD patterns for BSCFW as-prepared, after annealing at 750 °C for 10 days in static air, annealing in flowing 1% CO_2 in Ar at 650 °C for 5 days, annealing at 650 °C for 7 days while vaporised Cr from steel 316 fired at 850 °C was passed over the sample at 650 °C by flowing humid air, and fired to the fabrication condition of 950 °C for 3 hours with a 1:1 mass ratio mixture with SDC. SDC peaks are marked with asterisks. (b) Synchrotron X-ray diffraction patterns for as-prepared BSCFW and after long-term ASR test at 650 °C for 60 hours in air. SDC peaks are marked with asterisks and Au peaks with arrows.

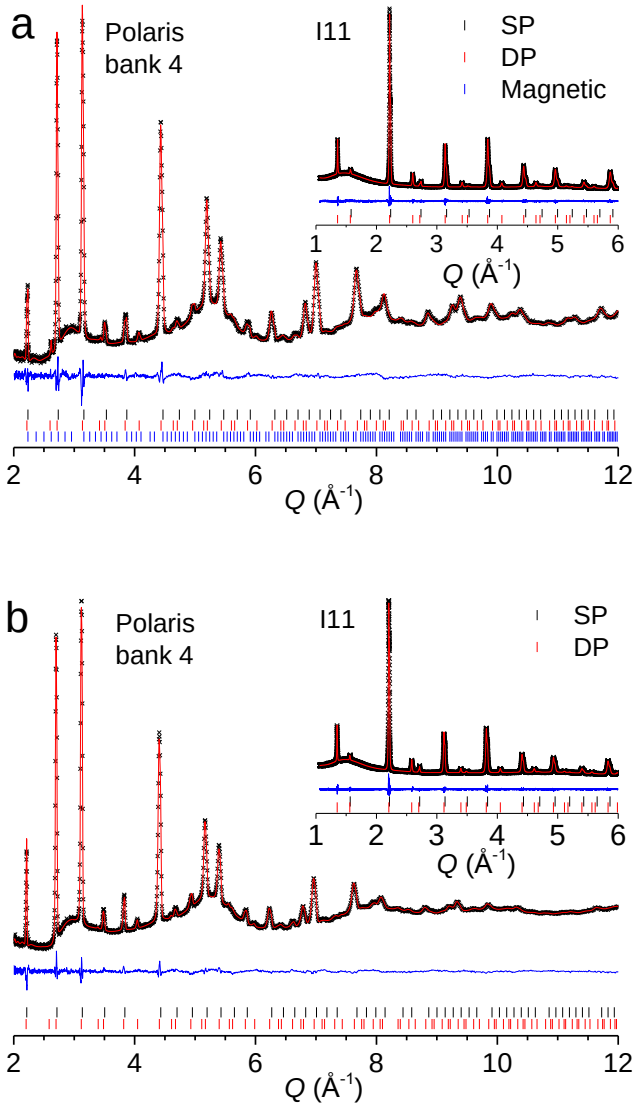

Figure 3: Rietveld refinement of BSCFW. Observed (cross), calculated (red), and difference (blue) profiles from combined Rietveld refinement of powder diffraction data of BSCFW. (a) At room temperature and (b) at 600 °C in flowing air. Tick marks show the Bragg reflections for the SP in black, DP in red and magnetic phase in blue. The reliability factors for the two perovskite phases in (a) are R_{wp} = 5.80%, R_{exp} = 3.77%, χ^2 = 2.38, R_{bragg}(SP) = 1.09%, R_{bragg}(DP) = 1.05% for I11; R_{wp} = 1.77%, R_{exp} = 1.09%, χ^2 = 2.64, R_{bragg}(SP) = 1.38%, R_{bragg}(DP) = 1.45% for Polaris bank 4; in (b) are R_{wp} = 5.75%, R_{exp} = 3.79%, χ^2 = 2.29, R_{bragg}(SP) = 0.68%, R_{bragg}(DP) = 1.00% for I11; R_{wp} = 1.07%, R_{exp} = 0.74%, χ^2 = 2.12, R_{bragg}(SP) = 2.20%, R_{bragg}(DP) = 0.88% for Polaris bank 4. The fit for banks 3 and 5 is presented in Supplementary Figure 4 and 5.

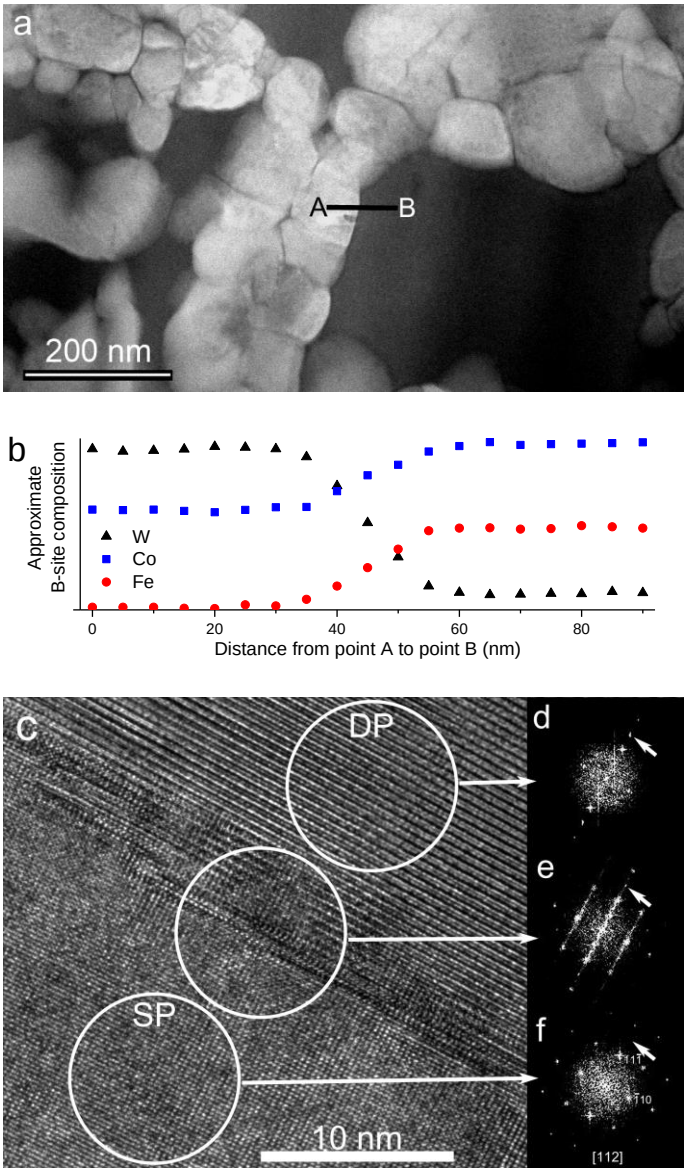

Figure 4: TEM studies of BSCFW. (a) Dark field image of BSCFW showing DP (light) and SP (dark) crystallites marked with point A in the DP and B in the SP crystallite (b) The line-scan EDS from points A to B indicates the compositional difference between two phases. (c) HRTEM image of the interface between an SP grain, oriented on [112] zone axes, and a DP grain, along with Fast Fourier Transforms (FFT) generated from selected areas, indicated by circles. (d) Upper part of the interface is indexed as DP while (f) lower part as SP which was clearly evidenced by the absence of superstructure spots indicated by arrows. (e) The FT of the interface is exact overlap of the FFT of two phases which suggests that two crystallites are aligned and coherent.

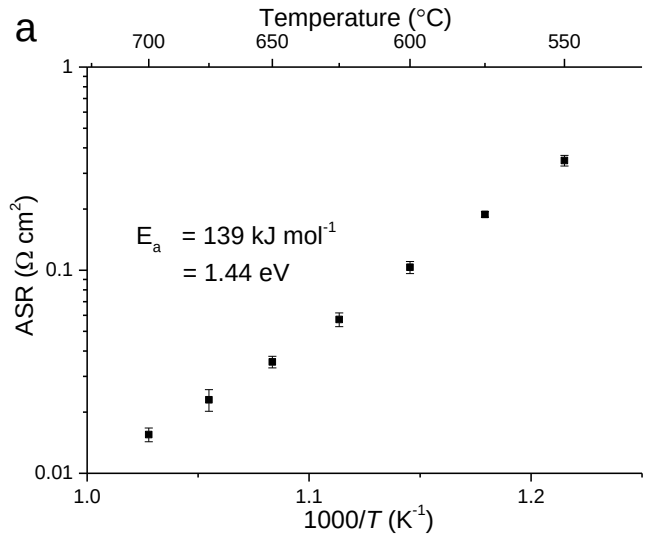
a
Temperature (°C)
700
650
600
550
1
0.1
0.01
ASR (Ω cm²)
E_a = 139 kJ mol⁻¹
= 1.44 eV
1.0
1.1
1.2
1000/T (K⁻¹)

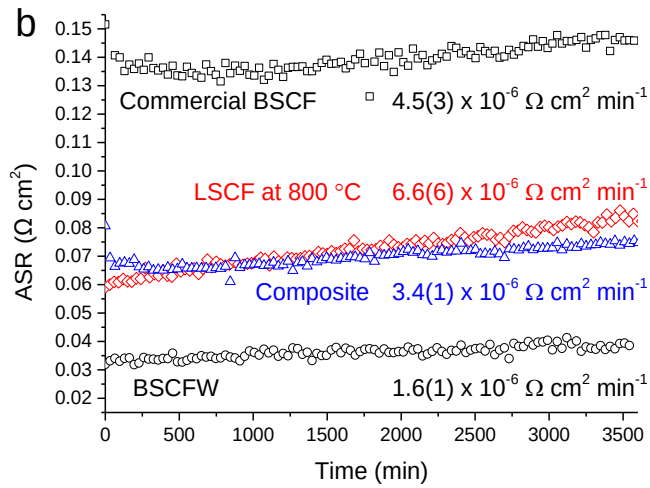
b
0.15
0.14
0.13
0.12
0.11
0.10
0.09
0.08
0.07
0.06
0.05
0.04
0.03
0.02
ASR (Ω cm²)
Commercial BSCF
4.5(3) x 10⁻⁶ Ω cm² min⁻¹
LSCF at 800 °C
6.6(6) x 10⁻⁶ Ω cm² min⁻¹
Composite
3.4(1) x 10⁻⁶ Ω cm² min⁻¹
BSCFW
1.6(1) x 10⁻⁶ Ω cm² min⁻¹
0
500
1000
1500
2000
2500
3000
3500
Time (min)

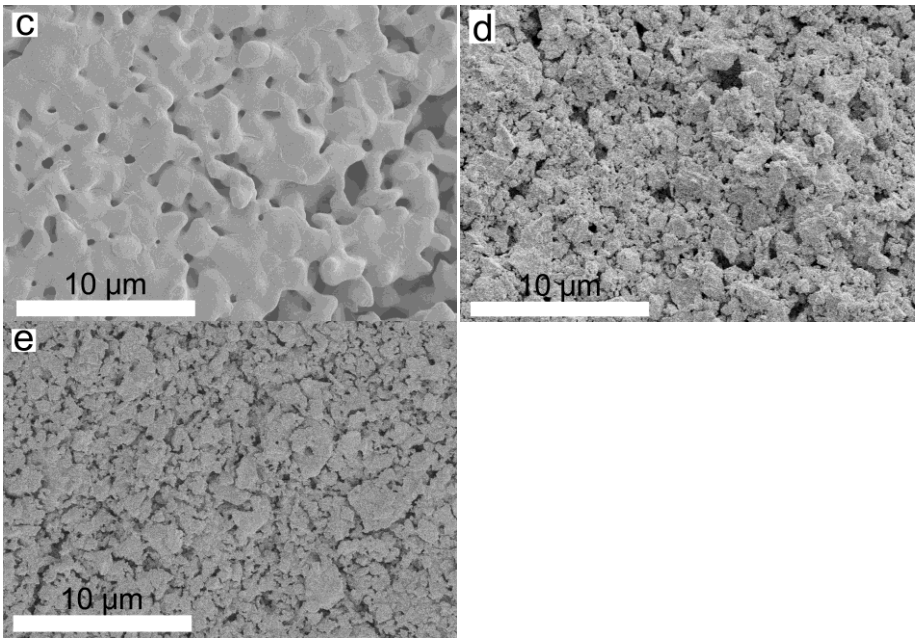
c
10 µm
d
10 µm
e
10 µm

Figure 5: ASR and SEM micrographs for BSCFW and other materials. ASR of BSCFW (a) in static air versus temperature and (b) at 650 °C in static air over 60 hours for BSCFW (black circle), commercial BSCF (black square) and a physically-mixed composite of pre-prepared BSCF and $BaSrCoWO_6$ with 30:70 wt. ratio (blue triangle) along with ASR of commercial LSCF on gadolinium doped ceria electrolyte at 800 °C (red diamond) which is plotted for comparison. All prepared with the same fabrication method and gradients for the plots are also presented. Typical complex impedance plots for BSCFW are shown in Supplementary Figure 8. SEM micrographs for c) BSCF, d) BSCFW and e) a physically-mixed composite of BSCF and $BaSrCoWO_6$ in 30:70 wt. ratio, all fabricated on SDC electrolytes following the same protocol. Their estimated porosities are 22, 33 and 34% respectively. The error bars in (a) represent three standard deviations for the measurement of three samples.